Article

Small Signal Modeling of LLC Converter with LED Load and Quasi-Resonant Controller Based Active Ripple Rejection

Xiao Long [1,2,*] and **Dongdong Chen** [1,2]

1. School of Electrical and Electrical Engineering, Minnan University of Science and Technology, Quanzhou 362700, China
2. Key Laboratory of Industrial Automation Control Technology and Application of Fujian Higher Education, Quanzhou 362700, China
* Correspondence: xdragonl2015@zju.edu.cn

Abstract: This paper has analyzed the defects of the traditional extended description function (EDF) based LLC small signal modeling method when driving light emitting diode (LED) load and proposed an accuracy improvement method. Detailed small signal model modeling methods have been deduced, and the accuracy of different modeling methods has been compared thoroughly. To suppress the second-order harmonic ripple in the direct current link-induced output current ripple, a quasi-resonant controller (QRC) is adopted to realize active ripple rejection (ARR). Considering the frequency of the second-order harmonic ripple changes with the grid voltage frequency, a single-phase software phase lock loop (SPLL) is adopted to extract the frequency of the second-order harmonic. By dynamically regulating the control parameter of the QRC according to the locked second-order frequency, output voltage ripple active rejection ability immune to grid voltage frequency deviation is obtained. Based on the deduced accurate small signal model, the digital controller is designed with stability, steady state and dynamics performance guaranteed. The accuracy of the proposed small signal model, the SPLL and the QRC-based ARR method has been verified at last.

Keywords: LLC converter; small signal modeling; active ripple rejection; quasi-resonant controller; SPLL

1. Introduction

LLC resonant converter possesses the merits of voltage isolation, voltage regulation ability, soft witching with zero voltage switch (ZVS) for the transformer primary power semiconductor devices and zero current switch (ZCS) for the transformer secondary power rectifiers, which make it prevalent in the applications of LED driver, data center power supply, household electrical, electrical vehicle charger and so on [1–5].

Generally, the design work of the LLC converter can be divided into the resonant parameter design and the digital controller design. First, the harmonic approximation (FHA) method is largely adopted for the design of resonant parameters according to the voltage regulation requirement, acceptable frequency variation range, ZVS, maximal allowed resonant frequency and other design restraints [6,7]. As to the design of the digital controller, the LLC small signal model should be deduced first. In most cases, the key control object of the LLC converter is to keep the output voltage constant, and the output load is treated as a pure resistance. Based on this assumption, many extend the description function based small signal models of the deduced LLC converter [8–11].

However, for LLC converter driving LED, the load is highly nonlinear. Besides, the control objective is to regulate the output current but not to keep the output voltage constant. Thus, the traditional EDF small signal modeling method treating the output load as pure resistance is not accurate enough. The authors of [10] treated the LED load as a power equivalent resistance load and established the small signal model of the LLC LED driver by the traditional EDF as in [8,9]. As has been verified by the authors of [11], owing to

the nonlinear LED load, the deduced output current to normalized switching frequency small signal model in [10] is not accurate. By considering the nonlinear model of LED load, the authors of [11] have constructed an accurate small signal model of LLC converter with LED load. However, the problem that the traditional resistance equivalent model is not accurate has not been solved by the authors of [11]. This paper has analyzed the defects of the traditional EDF-based small signal modeling method when driving LED load, and the accuracy of the small signal model has been improved by calculating the transfer function using the internal resistance of LED load but not output power equivalent resistance. The accuracy of the improved EDF modeling method for LED load has been verified by small signal frequency response experiments. Based on the accurate small signal model, the compensation controller is designed with stability, steady state and dynamic performance obtained.

To promote the reliability and duration of the off-line LED driver system, a high lifetime film capacitor in the direct current (DC) input port is gradually replaced by the electrolytic capacitor [12,13]. In most cases, the DC input terminal of the LLC LED driver is powered by a single-phase boost-type power factor correction (PFC) power supply, due to the low capacitance of the film capacitor, the DC output voltage ripple of PFC with film capacitor as filtering and supporting capacitor is larger than that of electrolytic capacitor. Furthermore, the main harmonic of the voltage ripple is the secondary order harmonic [14,15]. Due to the small internal resistance of LED, without proper control, DC link voltage ripple-induced LLC converter output voltage ripple will cause a large current ripple, which will cause an unacceptable flicker. To solve this problem, a quasi-resonant controller (QRC) as in [16,17] is adopted to realize active ripple rejection (ARR). As the gain of the QRC decreases sharply once grid voltage frequency shifting happens, a frequency adaptive single-phase software phase lock loop (SPLL) as in [18,19] is adopted to lock the grid voltage frequency. By dynamically tracing the frequency of the input voltage ripple and regulating the control parameter of the QRC, the best ARR performance is realized. The correctness of the designed SPLL and the QRC-based ARR method has been verified by simulation results.

The remaining content of the paper is arranged as follows. Section 2 discusses the EDF-based LLC LED driving converter small signal modeling method, analyzes the defects of the power equivalent resistance-based model, and constructs the transfer function between the output current and the normalized switching frequency. The compensator controller and output current ripple rejection controller are detailed in Section 3. The correctness of the proposed close-loop controller is verified in Section 4. The conclusion is given in Section 5.

2. Small Signal Model of LLC Converter with LED Load

The typical circuit diagram of a half-bridge LLC LED driver is shown in Figure 1, where voltage V_{ab} represents the half-bridge input quasi-square wave voltage and its peak voltage equals the input DC input voltage V_{in}. L_r and C_r represent the resonant inductance and capacitance, respectively, and r_s is the parasitic resistance of the resonant loop. L_m is the magnetizing inductance and the transfer ratio of the transformer is N:1:1. D_1 and D_2 are rectifier diodes connected to the center-tapped secondary coil of the transformer. C_o is output filter capacitance and r_c is its parasitic resistance. V_o and r_d represent output voltage and LED diode internal resistance, respectively. i_r, i_m, i_p and i_s are resonant current, magnetizing current, transformer primary side current and rectifier current, respectively. P_o is the nominal output power. R_o is the output power equivalent load resistance, which will be used as the output load resistance in the following traditional EDF-based LLC LED driver small signal model. The main circuit parameter values are designed based on the FHA method and are given in Table 1.
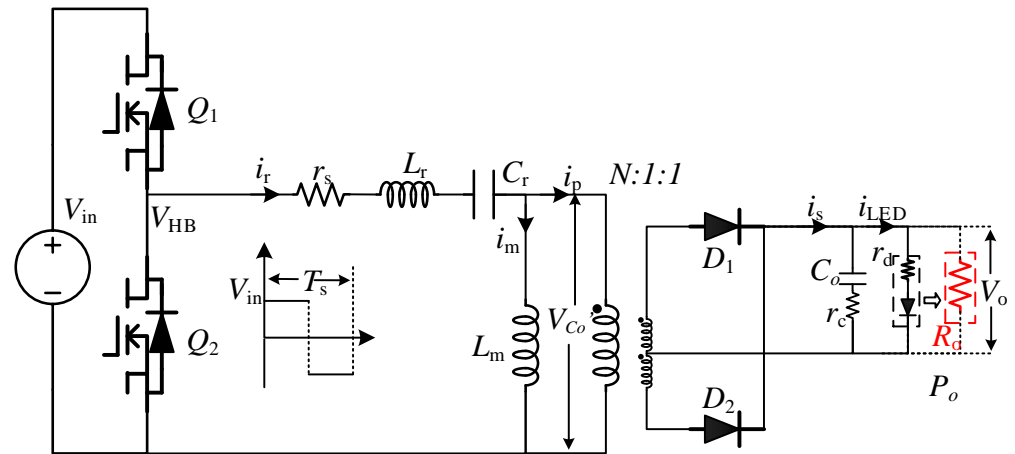
Figure 1. Circuit diagram of half-bridge LLC converter. The resistance boxed by dotted red line represented the output power equivalent resistance R_o.

Table 1. Main circuit parameter values.

L_r	253 uH	V_{th}	80 V
C_r	10 nF	r_d	6.2
L_m	760 uH	r_c	50 m
N	2.3	C_o	10 uF
r_s	0.1 Ω	P_o	100 W
f_r	100 kHz	V_{in}	400 V

2.1. Traditional EDF-Based LLC LED Driving Small Signal Modeling

As has been pointed out in Section 1, the analytical method to obtain a small signal model of the LLC converter is the EDF method. The deduction of the traditional EDF method can be divided into the following six steps.

2.1.1. Nonlinear Circuit Equations

The first step of the EDF method is listing the nonlinear equations of the LLC converter based on Kirchhoff voltage and current laws. In the traditional EDF modeling method, LED load is treated as an output power equivalent resistance R_o which equals V_o^2/P_o. According to the half-bridge circuit diagram shown in Figure 1, Equations (1)–(5) can be deduced.

$$v_{ab} = L_r \frac{di_r}{dt} + i_r r_s + v_{Cr} + \text{sgn}(i_p)V'_{Co} \tag{1}$$

where

$$\text{sgn}(i_p) = \begin{cases} -1, if\,(i_p < 0) \\ +1, if\,(i_p \geq 0) \end{cases}$$

$$i_r = C_r \frac{dv_{Cr}}{dt} \tag{2}$$

The equivalent output voltage V_{Co}' at the transformer's primary side is

$$\text{sgn}(i_p)v'_{C_o} = L_m \frac{di_m}{dt} \tag{3}$$

The relationship between the rectifier current i_s and the output capacitance voltage v_{Co} is

$$i_s = \left(1 + \frac{r_c}{R_o}\right)C_o \frac{dv_{C_o}}{dt} + \frac{v_{C_o}}{R_o} \tag{4}$$

According to (4), output voltage v_o can be represented as:

$$v_o = r_c' i_s + \frac{r_c'}{r_c} v_{C_o} \tag{5}$$

where $r_c' = r_c \| R_o$.

2.1.2. DC and First-Order Harmonic Approximation

In the second step, state variables are approximated by their fundamental sin and cos components. Resonant current i_r, magnetizing current i_m and resonant capacitor voltage v_{Cr} can be approximated by their fundamental harmonic as shown in Equations (6)–(8), respectively:

$$i_r(t) = i_{rs}(t) \sin \omega_s t - i_{rc}(t) \cos \omega_s t \tag{6}$$

where ω_s is the switching angular frequency.

$$i_m(t) = i_{ms}(t) \sin \omega_s t - i_{mc}(t) \cos \omega_s t \tag{7}$$

In Equations (6) and (7), i_{rs} (i_{ms}) and i_{rc} (i_{mc}) are the amplitudes of resonant current i_r (magnetizing current i_m) fundamental sine and cosine components.

$$v_{C_r}(t) = V_{in}/2 + v_{cs}(t) \sin \omega_s t - v_{cc}(t) \cos \omega_s t \tag{8}$$

In Equation (8), $V_{in}/2$ is the DC bias component, and v_{cs} and v_{cc} are the amplitudes of resonant capacitance voltage v_{Cr} fundamental sine and cosine components.

2.1.3. Extended Description Function

The third step is the most important step because, in this step nonlinear variables in the circuit, equations are approximated by the DC and fundamental sin and cos components of state variables. The nonlinear terms in Equations (1) and (5) such as sgn(i_p)*v_{Co}', v_{ab} and i_s can be approximated by their fundamental and DC terms as shown in Equations (9)–(11).

$$v_{ab} = V_{in}/2 + f_1(d, V_{dc}) \sin(\omega_s t) \tag{9}$$

$$\text{sgn}(i_p) v_{C_o}' = f_2(i_{ss}, i_s, v_{C_o}') \sin \omega_s t - f_3(i_{sc}, i_s, v_{C_o}') \cos \omega_s t \tag{10}$$

$$i_s = f_4(i_{ss}, i_{sc}) \tag{11}$$

In Equation (9), the first-order harmonics amplitude $f_1(d, v_{dc})$ can be calculated by the Fourier series expansion method as given in Equation (12).

$$f_1(d, v_{dc}) = \frac{2V_{in}}{\pi} \sin\left(\frac{\pi}{2} d\right) = v_{is} \tag{12}$$

where d is the duty ratio of half one switch cycle, and v_{is} is the first-order sine component of the resonant tank input voltage. The transformer's primary voltage is also a triangle waveform with zero dc component, and its first-order harmonic is in phase with the primary winding current. By the EDF method, the sine and cosine components of the transformer's primary voltage can be represented by Equations (13) and (14), respectively.

$$f_2(i_{ss}, i_{sp}, v_{C_o}') = \frac{4}{\pi} \frac{i_{ps}}{i_{pp}} v_{C_o}' = \frac{4n}{\pi} \frac{i_{ps}}{i_{pp}} v_{C_o} = v_{ps} \tag{13}$$

$$f_3(i_{sc}, i_{sp}, v_{C_o}') = \frac{4}{\pi} \frac{i_{pc}}{i_{pp}} v_{C_o}' = \frac{4n}{\pi} \frac{i_{pc}}{i_{pp}} v_{C_o} = v_{pc} \tag{14}$$

where i_{ss} and i_{sc} are the sine and cosine components of the transformer's secondary current. v_{ps} and v_{pc} are the sine and cosine components of the transformer's primary voltage. i_{ps} and i_{pc} are the sine and cosine components of the transformer primary current, and i_{pp} is the root mean square value of the transformer primary current first order harmonic sine and cosine amplitudes as in Equation (15).

$$i_{pp} = \sqrt{i_{ps}^2 + i_{pc}^2} \tag{15}$$

2.1.4. Harmonic Balance Method

In the fourth step, by substituting the state variables and nonlinear variables into the nonlinear equations and adopting the harmonics balance method, the nonlinear large-signal model of the LLC converter can be deduced.

Substituting Equations (6)–(15) into Equations (1)–(5), the corresponding DC, sine and cosine terms are balanced, respectively. Thus, Equations (16)–(23) can be obtained.

$$v_{is} = L_r \left(\frac{di_{rs}}{dt} + \omega_s i_{rc} \right) + r_s i_{rs} + v_{cs} + v_{ps} \tag{16}$$

$$0 = L_r \left(\frac{di_{rc}}{dt} - \omega_s i_{rs} \right) + r_s i_{rc} + v_{cc} + v_{pc} \tag{17}$$

$$i_{rs} = C_r \left(\frac{dv_{cs}}{dt} + \omega_s v_{cc} \right) \tag{18}$$

$$i_{rc} = C_r \left(\frac{dv_{cc}}{dt} - \omega_s v_{cs} \right) \tag{19}$$

$$v_{ps} = L_m \left(\frac{di_{ms}}{dt} + \omega_s i_{mc} \right) \tag{20}$$

$$v_{pc} = L_m \left(\frac{di_{mc}}{dt} - \omega_s i_{ms} \right) \tag{21}$$

$$\frac{2n}{\pi} i_{pp} = \left(1 + \frac{r_c}{R_o} \right) C_o \frac{dv_{C_o}}{dt} + \frac{v_{C_o}}{R_o} \tag{22}$$

$$v_o = r_c' \frac{2n}{\pi} i_{pp} + \frac{r_c'}{r_c} v_{C_o} \tag{23}$$

2.1.5. Steady-State Working Point Calculation

Next, by assuming the deviation of state variables to be zero, the steady state working point can be calculated in the fifth step. Under the condition that the output power keeps constant, the output resistance R_o can be transferred to the transformer's primary side, and the equivalent resistance R_e is given in Equation (24).

$$R_e = \frac{8n^2}{\pi^2} R_o \tag{24}$$

According to Equation (22), Equation (25) can be calculated as:

$$v_{C_o}' = n v_{C_o} = \frac{\pi}{4} i_{pp} R_e \tag{25}$$

Taking (25) into Equations (13) and (14), Equation (26) can be calculated:

$$\begin{cases} V_{ps} = I_{ps} R_e \\ V_{pc} = I_{pc} R_e \end{cases} \tag{26}$$

According to KCL and harmonics balance, the relationship between sine and cosine components of resonant current i_r, magnetizing current i_m and transformer primary current i_p is given in Equation (27).

$$\begin{cases} I_{ps} = I_{rs} - I_{ms} \\ I_{pc} = I_{rc} - I_{mc} \end{cases} \tag{27}$$

When working in steady state, the state variables in Equations (16)–(23) do not change with time. By setting the time derivatives to be zero, the steady-state operation point can be calculated as shown in Equations (28)–(31). In (28), as d is the duty ratio of half one switching cycle, the steady state value D equals one.

$$\begin{cases} \frac{2V_{dc}}{\pi} \sin\left(\frac{\pi}{2}D\right) = L_r\Omega_s I_{rc} + r_s I_{rs} + V_{cs} + I_{ps}R_e \\ 0 = -L_r\Omega_s I_{rs} + r_s I_{rc} + V_{cc} + I_{pc}R_e \end{cases} \tag{28}$$

$$\begin{cases} I_{rs} = C_r\Omega_s V_{cc} \\ I_{rc} = -C_r\Omega_s V_{cs} \end{cases} \tag{29}$$

$$\begin{cases} V_{ps} = L_m\Omega_s I_{mc} \\ V_{pc} = -L_m\Omega_s I_{ms} \end{cases} \tag{30}$$

$$V_{C_o} = \frac{2n}{\pi} I_{pp} R \tag{31}$$

To calculate the steady state working point, it is better to represent Equations (24)–(31) in matrix form as shown in Equation (32).

$$E \cdot X = U \tag{32}$$

where steady state variable vector $X = [I_{rs}, I_{rc}, V_{cs}, V_{cc}, I_{ms}, I_{mc}]^{\mathrm{T}}$, input variable vector $U = [V_{is}, 0, 0, 0, 0, 0]^{\mathrm{T}}$, and coefficient matrix E is given in Equation (33).

$$E = \begin{bmatrix} r_s + R_e & L_r\Omega_s & 1 & 0 & -R_e & 0 \\ -L_r\Omega_s & r_s + R_e & 0 & 1 & 0 & -R_e \\ 1 & 0 & 0 & -C_r\Omega_s & 0 & 0 \\ 0 & 1 & C_r\Omega_s & 0 & 0 & 0 \\ R_e & 0 & 0 & 0 & -R_e & -L_m\Omega_s \\ 0 & R_e & 0 & 0 & L_m\Omega_s & -R_e \end{bmatrix} \tag{33}$$

Then steady state working point can be calculated by matrix manipulation as in Equation (34).

$$X = E^{-1} \cdot U \tag{34}$$

2.1.6. Small Signal Perturbation

At last, based on the calculated steady-state working point, the small signal model of the LLC converter can be deduced by small signal perturbation nearby the steady-state working point.

To obtain the small signal model of the full bridge LLC converter, perturbation and linearization in Equation (34) should be taken at the steady state working point.

$$\begin{aligned} &i_{rs} = I_{rs} + \hat{i}_{rs} \qquad i_{rc} = I_{rc} + \hat{i}_{rc} \\ &v_{ps} = V_{ps} + \hat{v}_{ps} \qquad v_{pc} = V_{pc} + \hat{v}_{pc} \\ &v_{cs} = V_{cs} + \hat{v}_{cs} \qquad v_{cc} = V_{cc} + \hat{v}_{cc} \\ &i_{ms} = I_{ms} + \hat{i}_{ms} \qquad i_{mc} = I_{mc} + \hat{i}_{mc} \\ &v_{dc} = V_{dc} + \hat{v}_{dc} \qquad v_{C_o} = V_{C_o} + \hat{v}_{C_o} \\ &d = D + \hat{d} \qquad \omega_s = \Omega_s + \omega_r\hat{\omega}_s/\omega_r = \Omega_s + \omega_r\hat{\omega}_{sN} \end{aligned} \tag{35}$$

where ω_r is the resonant angular frequency, and $\hat{\omega}_{rN}$ is the switching angular frequency perturbation normalized to ω_r.

By substituting Equation (35) into the large signal model of Equations (16)–(23) and eliminating the steady-state working point, the small signal model of the full bridge LLC converter can be obtained as follows:

$$
\begin{cases}
\dfrac{d\hat{i}_{rs}}{dt} = -\dfrac{r_s+H_{ips}}{L_r}\hat{i}_{rs} - \dfrac{L_r\Omega_s+H_{ipc}}{L_r}\hat{i}_{rc} + \dfrac{H_{ips}}{L_r}\hat{i}_{ms} + \dfrac{H_{ipc}}{L_r}\hat{i}_{mc} - I_{rc}\omega_r\hat{\omega}_{sN} \\
\qquad - \dfrac{\hat{v}_{cs}}{L_r} - \dfrac{H_{vps}}{L_r}\hat{v}_{C_o} + \dfrac{K_1}{L_r}\hat{v}_{dc} + \dfrac{K_2}{L_r}\hat{d} \\
\dfrac{d\hat{i}_{rc}}{dt} = \dfrac{L_r\Omega_s-G_{ips}}{L_r}\hat{i}_{rs} - \dfrac{r_s+G_{ipc}}{L_r}\hat{i}_{rc} + \dfrac{G_{ips}}{L_r}\hat{i}_{ms} + \dfrac{G_{ipc}}{L_r}\hat{i}_{mc} + I_{rs}\omega_r\hat{\omega}_{sN} \\
\qquad - \dfrac{\hat{v}_{cc}}{L_r} - \dfrac{G_{vpc}}{L_r}\hat{v}_{C_o}
\end{cases}
\tag{36}
$$

$$
\begin{cases}
\dfrac{d\hat{v}_{cs}}{dt} = -\Omega_s\hat{v}_{cc} - V_{cc}\omega_r\hat{\omega}_{sN} + \dfrac{\hat{i}_{rs}}{C_r} \\
\dfrac{d\hat{v}_{cc}}{dt} = \Omega_s\hat{v}_{cs} + V_{cs}\omega_r\hat{\omega}_{sN} + \dfrac{\hat{i}_{rc}}{C_r}
\end{cases}
\tag{37}
$$

$$
\begin{cases}
\dfrac{d\hat{i}_{ms}}{dt} = \dfrac{H_{ips}}{L_m}\hat{i}_{rs} + \dfrac{H_{ipc}}{L_m}\hat{i}_{rc} - \dfrac{H_{ips}}{L_m}\hat{i}_{ms} - \dfrac{L_m\Omega_s+H_{ipc}}{L_m}\hat{i}_{mc} + \dfrac{H_{vps}}{L_m}\hat{v}_{C_o} - I_{mc}\omega_r\hat{\omega}_{sN} \\
\dfrac{d\hat{i}_{mc}}{dt} = \dfrac{G_{ips}}{L_m}\hat{i}_{rs} + \dfrac{G_{ipc}}{L_m}\hat{i}_{rc} + \dfrac{L_m\Omega_s-G_{ips}}{L_m}\hat{i}_{ms} - \dfrac{G_{ipc}}{L_m}\hat{i}_{mc} + \dfrac{G_{vpc}}{L_m}\hat{v}_{C_o} + I_{ms}\omega_r\hat{\omega}_{sN}
\end{cases}
\tag{38}
$$

$$
\begin{cases}
\dfrac{d\hat{v}_{C_o}}{dt} = \dfrac{R_oK_{ips}}{(R_o+r_c)C_o}\hat{i}_{rs} + \dfrac{R_oK_{ipc}}{(R_o+r_c)C_o}\hat{i}_{rc} - \dfrac{R_oK_{ips}}{(R_o+r_c)C_o}\hat{i}_{ms} - \dfrac{R_oK_{ipc}}{(R_o+r_c)C_o}\hat{i}_{mc} - \dfrac{1}{(R_o+r_c)C_o}\hat{v}_{C_o} \\
\hat{v}_o = r'_cK_{ips}\left(\hat{i}_{rs} - \hat{i}_{ms}\right) + r'_cK_{ipc}\left(\hat{i}_{rc} - \hat{i}_{mc}\right) + \dfrac{r'_c}{r_c}\hat{v}_{C_o}
\end{cases}
\tag{39}
$$

where, coefficients H_{ipc}, H_{ips}, H_{vps}, G_{ipc}, G_{ips}, G_{vps}, K_{ips}, K_{ipc}, K_1 and K_2 are defined in the equation below.

$$
\begin{cases}
H_{ips} = \dfrac{4n}{\pi}\dfrac{I_{pc}^2}{I_{pp}^3}V_{C_o}, \quad H_{ipc} = -\dfrac{4n}{\pi}\dfrac{I_{ps}I_{pc}}{I_{pp}^3}V_{C_o}, \quad H_{vps} = \dfrac{4n}{\pi}\dfrac{I_{ps}}{I_{pp}}, \\
G_{ips} = -\dfrac{4n}{\pi}\dfrac{I_{ps}I_{pc}}{I_{pp}^3}V_{C_o}, \quad G_{ipc} = \dfrac{4n}{\pi}\dfrac{I_{ps}^2}{I_{pp}^3}V_{C_o}, \quad H_{vps} = \dfrac{4n}{\pi}\dfrac{I_{pc}}{I_{pp}} \\
K_1 = \dfrac{2}{\pi}\sin\dfrac{D\pi}{2}, \quad K_2 = V_{in}\cos\dfrac{D\pi}{2} \\
K_{ips} = \dfrac{2n}{\pi}\dfrac{I_{ps}}{I_{pp}}, K_{ipc} = \dfrac{2n}{\pi}\dfrac{I_{pc}}{I_{pp}}
\end{cases}
\tag{40}
$$

According to Equations (36)–(40), the state space small signal model of the full bridge LLC model can be deduced as shown in Equation (41).

$$
\begin{cases}
\dot{\hat{x}} = A\hat{x} + Bu \\
y = C\hat{x}
\end{cases}
\tag{41}
$$

where state variable vector $\hat{x} = [\hat{i}_{rs}, \hat{i}_{rc}, \hat{v}_{cs}, \hat{v}_{cc}, \hat{i}_{ms}, \hat{i}_{mc}, \hat{v}_{C_o}]$, input state variable vector $u = [\hat{v}_{dc}, \hat{d}, \hat{\omega}_{sN}]$, output variable $y = \hat{v}_o$, and coefficient matrix A, B and C in Equation (41) are illustrated in Equations (42)–(44), respectively.

$$
A = \begin{bmatrix}
-\dfrac{r_s+H_{ips}}{L_r} & -\dfrac{L_r\Omega_s+H_{ipc}}{L_r} & -\dfrac{1}{L_r} & 0 & \dfrac{H_{ips}}{L_r} & \dfrac{H_{ipc}}{L_r} & -\dfrac{H_{vps}}{L_r} \\
\dfrac{L_r\Omega_s-G_{ips}}{L_r} & -\dfrac{r_s+G_{ipc}}{L_r} & 0 & -\dfrac{1}{L_r} & \dfrac{G_{ips}}{L_r} & \dfrac{G_{ipc}}{L_r} & -\dfrac{G_{vpc}}{L_r} \\
\dfrac{1}{C_r} & 0 & 0 & -\Omega_s & 0 & 0 & 0 \\
0 & \dfrac{1}{C_r} & \Omega_s & 0 & 0 & 0 & 0 \\
\dfrac{H_{ips}}{L_m} & \dfrac{H_{ipc}}{L_m} & 0 & 0 & -\dfrac{H_{ips}}{L_m} & -\dfrac{L_m\Omega_s+H_{ipc}}{L_m} & \dfrac{H_{vps}}{L_m} \\
\dfrac{G_{ips}}{L_m} & \dfrac{G_{ipc}}{L_m} & 0 & 0 & \dfrac{L_m\Omega_s-G_{ips}}{L_m} & -\dfrac{G_{ipc}}{L_m} & \dfrac{G_{vpc}}{L_m} \\
\dfrac{R_oK_{ips}}{(R_o+r_c)C_o} & \dfrac{R_oK_{ipc}}{(R_o+r_c)C_o} & 0 & 0 & -\dfrac{R_oK_{ips}}{(R_o+r_c)C_o} & -\dfrac{R_oK_{ipc}}{(R_o+r_c)C_o} & -\dfrac{1}{(R_o+r_c)C_o}
\end{bmatrix}
\tag{42}
$$

$$B = \begin{bmatrix} \frac{K_1}{L_r} & \frac{K_2}{L_r} & -I_{rc}\omega_r \\ 0 & 0 & I_{rs}\omega_r \\ 0 & 0 & -V_{cc}\omega_r \\ 0 & 0 & V_{cs}\omega_r \\ 0 & 0 & -I_{mc}\omega_r \\ 0 & 0 & I_{ms}\omega_r \\ 0 & 0 & 0 \end{bmatrix} \tag{43}$$

$$C = \begin{bmatrix} r'_c K_{i_{ps}} & r'_c K_{i_{pc}} & 0 & 0 & -r'_c K_{i_{ps}} & -r'_c K_{i_{pc}} & \frac{r'_c}{r_c} \end{bmatrix} \tag{44}$$

Based on Equation (41), the transfer function $\hat{v}_o / \hat{f}_{sN}$ of the half-bridge LLC converter is deduced in Equation (45).

$$G(s) = C(s \cdot I - A)^{-1} B \tag{45}$$

where matrix *I* is a unit matrix.

The traditional EDF-based LLC converter small signal model deducing method treats the load as a resistance Ro. After obtaining the transfer function $\hat{v}_o / \hat{f}_{sN}$ in Equation (45), the output current to normalized switching frequency transfer function i_{LED}/f_{sN} is calculated by Equation (46). For simplicity, this traditional EDF-based LLC LED driver small signal modeling method is denoted by R_{eq}-R_o.

$$\frac{i_{LED}}{f_{sN}} = \frac{\hat{v}_o}{\hat{f}_{sN} \cdot R_o} \tag{46}$$

However, the R_{eq}-R_o method has ignored the nonlinearity of LED load. There will be current flowing through the LED load once the positive bias voltage exceeds the threshold voltage v_{th}. Thus, to improve the accuracy of the transfer function i_{LED}/f_{sN}, Equation (47) should be adopted, where r_d is LED internal parasitic resistance. For simplicity, this improved EDF-based LLC LED driver small signal modeling method is denoted by R_{eq}-r_d.

$$\frac{i_{LED}}{f_{sN}} = \frac{\hat{v}_o}{\hat{f}_{sN} \cdot r_d} \tag{47}$$

Comparing Equations (46) and (47), it can be seen that the gain calculated by (46) is not accurate. The larger the difference between R_o and r_d is, the bigger the DC gain error calculated by Equation (46) is.

2.2. Improved EDF-Based LLC LED Driving Small Signal Modeling

Though R_{eq}-r_d method has improved the DC gain accuracy of the calculated transfer function i_{LED}/f_{sN}. It is still based on the traditional R_{eq}-R_o method. The nonlinearity of LED load has not been taken into consideration during the deduction of the small signal model. To improve the accuracy of the transfer function i_{LED}/f_{sN}, the output power equivalent resistance load model should be replaced by the LED nonlinear model. For simplicity, this LED nonlinear model and EDF-based LLC LED driver small signal modeling method is denoted by i_{LED}.

The first step is listing the nonlinear circuit equations. By simple circuit analysis, LED current i_{LED} can be calculated by Equation (48). The terminal voltage v_{LED} of LED is calculated by Equation (49), and the rectified current i_s at the transformer secondary side is given in Equation (50).

$$i_{LED} = \frac{r'_c}{r_d} i_s + \frac{v_{C_o}}{r_c + r_d} - \frac{v_{th}}{r_c + r_d} \tag{48}$$

$$v_{LED} = i_{LED} \cdot r_d + V_{th} = v_{C_o} + r_c \frac{dv_{C_o}}{dt} \tag{49}$$

$$i_s = C_o \frac{dv_{C_o}}{dt}\left(1 + \frac{r_c}{r_d}\right) + \frac{v_{C_o}}{r_d} - \frac{V_{th}}{r_d} \tag{50}$$

where $r_c' = r_C // r_d$.

Taking Equation (50) into Equation (49), v_{LED} can be deduced by Equation (51).

$$v_{LED} = i_s \cdot r_C' + \frac{r_C'}{r_d} v_{th} + \frac{r_C'}{r_c} v_{C_o} \tag{51}$$

The second and third steps are the same as the traditional EDF modeling method, Equations (6)–(15) can be used here. In the fourth step, Equations (16)–(21) are the same as the traditional EDF modeling method too. While Equation (22) is replaced by Equation (52).

$$\frac{2}{\pi} i_s = C_o \frac{dv_{C_o}}{dt}\left(1 + \frac{r_c}{r_d}\right) + \frac{v_{C_o}}{r_d} - \frac{V_{th}}{r_d} \tag{52}$$

In the next fifth step, the steady state working state can be deduced. According to Equations (48) and (51), steady state Equations (53) and (54) are derived.

$$I_{LED} = \frac{r_c'}{r_d} \frac{2nI_{pp}}{\pi} + \frac{V_{C_o}}{r_c + r_d} - \frac{V_{th}}{r_c + r_d} \tag{53}$$

$$V_{LED} = V_{C_o} = \frac{2n}{\pi} I_{pp} \cdot r_d + V_{th} \tag{54}$$

Taking (53) into Equations (16)–(21) and (52) and setting the deviation equaling zero, the steady state equations can be deduced as shown in Equations (55)–(57).

$$\begin{cases} \frac{2V_{dc}}{\pi}\sin\left(\frac{\pi}{2}D\right) = L_r\Omega_s I_{rc} + (r_s + R_{ac})I_{rs} + V_{cs} - I_{ps}R_{ac} + \frac{4n}{\pi}\frac{i_{ps}}{i_{pp}}V_{th} \\ 0 = -L_r\Omega_s I_{rs} + (r_s + R_{ac})I_{rc} + V_{cc} - I_{pc}R_{ac} + \frac{4n}{\pi}\frac{i_{pc}}{i_{pp}}V_{th} \end{cases} \tag{55}$$

$$\begin{cases} I_{rs} = C_r\Omega_s V_{cc} \\ I_{rc} = -C_r\Omega_s V_{cs} \end{cases} \tag{56}$$

$$\begin{cases} -R_{ac}I_{ps} + L_m\Omega_s I_{mc} - \frac{4n}{\pi}\frac{i_{ps}}{i_{pp}}V_{th} = 0 \\ R_{ac}I_{pc} + L_m\Omega_s I_{mc} + \frac{4n}{\pi}\frac{i_{pc}}{i_{pp}}V_{th} = 0 \end{cases} \tag{57}$$

where $R_{ac} = \frac{8n^2}{\pi^2} r_d$. According to Equations (55)–(57), the steady-state working points can be calculated by numerical calculation.

The last step is calculating the small signal transfer function by perturbation and linearization at the steady-state working point. The deduced state-space model of the LLC LED driver is given in Equation (58).

$$\begin{cases} \dot{\hat{x}} = A_1\hat{x} + B_1 u_1 \\ y_1 = C_1\hat{x} + Du_1 \end{cases} \tag{58}$$

where state variable vector $\hat{x} = [\hat{i}_{rs}, \hat{i}_{rc}, \hat{v}_{cs}, \hat{v}_{cc}, \hat{i}_{ms}, \hat{i}_{mc}, \hat{v}_{C_o}]$, input state variable vector $u_1 = [\hat{v}_{in}, \hat{v}_{th}, \hat{d}, \hat{\omega}_{sN}]$, output variable $y = \hat{i}_{LED}$, and coefficient matrix A_1, B_1, C_1 and D_1 in Equation (41) are illustrated in Equations (59)–(62), respectively.

$$A_1 = \begin{bmatrix}
-\frac{r_s + H_{ips}}{L_r} & -\frac{L_r\Omega_s + H_{ipc}}{L_r} & -\frac{1}{L_r} & 0 & \frac{H_{ips}}{L_r} & \frac{H_{ipc}}{L_r} & -\frac{H_{vps}}{L_r} \\
\frac{L_r\Omega_s - G_{ips}}{L_r} & -\frac{r_s + G_{ipc}}{L_r} & 0 & -\frac{1}{L_r} & \frac{G_{ips}}{L_r} & \frac{G_{ipc}}{L_r} & -\frac{G_{vpc}}{L_r} \\
\frac{1}{C_r} & 0 & 0 & -\Omega_s & 0 & 0 & 0 \\
0 & \frac{1}{C_r} & \Omega_s & 0 & 0 & 0 & 0 \\
\frac{H_{ips}}{L_m} & \frac{H_{ipc}}{L_m} & 0 & 0 & -\frac{H_{ips}}{L_m} & -\frac{L_m\Omega_s + H_{ipc}}{L_m} & \frac{H_{vps}}{L_m} \\
\frac{G_{ips}}{L_m} & \frac{G_{ipc}}{L_m} & 0 & 0 & \frac{L_m\Omega_s - G_{ips}}{L_m} & -\frac{G_{ipc}}{L_m} & \frac{G_{vps}}{L_m} \\
\frac{r_d K_{ips}}{(r_d + r_c)C_o} & \frac{r_d K_{ipc}}{(r_d + r_c)C_o} & 0 & 0 & -\frac{r_d K_{ips}}{(r_d + r_c)C_o} & -\frac{r_d K_{ipc}}{(r_d + r_c)C_o} & -\frac{1}{(r_d + r_c)C_o}
\end{bmatrix} \quad (59)$$

$$B_1 = \begin{bmatrix}
\frac{K_1}{L_r} & 0 & \frac{K_2}{L_r} & -I_{rc}\omega_r \\
0 & 0 & 0 & I_{rs}\omega_r \\
0 & 0 & 0 & -V_{cc}\omega_r \\
0 & 0 & 0 & V_{cs}\omega_r \\
0 & 0 & 0 & -I_{mc}\omega_r \\
0 & 0 & 0 & I_{ms}\omega_r \\
0 & \frac{1}{C_o(r_d + r_c)} & 0 & 0
\end{bmatrix} \quad (60)$$

$$C_1 = \begin{bmatrix} \frac{r_c' K_{ips}}{r_d} & \frac{r_c' K_{ipc}}{r_d} & 0 & 0 & \frac{-r_c' K_{ips}}{r_d} & \frac{-r_c' K_{ipc}}{r_d} & \frac{r_c'}{r_d r_c} \end{bmatrix} \quad (61)$$

$$D_1 = \begin{bmatrix} 0 & -\frac{1}{r_d + r_c} & 0 & 0 \end{bmatrix} \quad (62)$$

Based on Equation (58), the transfer function $\hat{i}_{LED}/\hat{f}_{sN}$ of the half-bridge LLC converter can be deduced from Equation (63).

$$G(s) = C_1(s \cdot I - A_1)^{-1} B_1 \quad (63)$$

where matrix I is a unit matrix.

2.3. Small Signal Model Accuracy Verification

Based on the circuit parameters given in Table 1, the bode diagrams of R_{eq}-R_o, R_{eq}-r_d and i_{LED} method-based transfer functions are illustrated in Figure 2. In addition, a frequency sweep experiment is conducted in a circuit simulator to obtain the accurate transfer function i_{LED}/f_{sN} curve as shown in Figure 2.
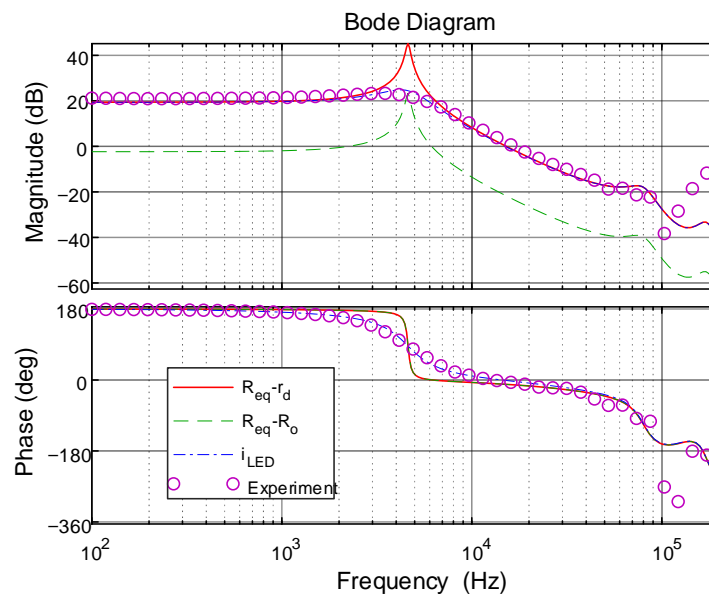

Figure 2. Bode diagram of four different transfer functions.

From Figure 2, it can be seen that:

(1) The Bode diagram of the transfer function (TF) i_{LED}/f_{sN} (shown by the curve i_{LED} in Figure 2) based on the LED nonlinear model is in consensus with that of frequency response experiment results (shown by the curve Experiment in Figure 2), which verify that the small signal model based on the LED nonlinear model has the highest accuracy.

(2) As in paper [3,4] and shown in Figure 2, TF i_{LED}/f_{sN} calculated by $v_o/f_{sN}/R_o$ (Bode diagram shown by the curve R_{eq}-R_o in Figure 2) causes the calculated open-loop gain much less than that of LED nonlinear model-based calculated TF. While the open-loop gain of the TF calculated by $v_o/f_{sN}/r_d$ (Bode diagram shown by the curve R_{eq}-r_d in Figure 2) is almost the same as that of LED nonlinear model based calculated TF as illustrated in Figure 2. This is because the threshold voltage of lighting LED is large and the power equivalent resistance R_o of LED is much greater than its internal resistance r_d. Thus, after obtaining TF v_o/f_{sN} between the output voltage v_o and the normalized switching frequency f_{sN} based on the power equivalent resistance model of LED, the TF i_{LED}/f_{sN} should be calculated by $v_o/f_{sN}/r_d$, not $v_o/f_{sN}/R_o$.

(3) As it has been verified that the calculated circuit DC working points are almost the same regardless of if the LED nonlinear model or the power equivalent resistance model is taken into account. In fact, the main difference between the LED nonlinear model and power equivalent resistance-based LLC converter small signal model comes from the load model itself. From Figure 2, it can be seen that the small internal resistance of LED has a significant impact on the damp ratio of the oscillation element with a pair of dominant complex poles in the TF i_{LED}/f_{sN}. The closer the internal resistance r_d is to the power equivalent resistance R_o, the more accurate the power equivalent resistance R_o based small signal model is.

Based on the circuit parameters given in Table 1, the LED nonlinear model-based TF i_{LED}/f_{sN} is deduced as given in Equation (64).

$$G_s(s) = \frac{5.8 \cdot 10^6 \left(s + 8.04 \cdot 10^8\right)\left(s - 5.178 \cdot 10^5\right)\left(s + 2 \cdot 10^6\right)\left(s^2 + 5.188 \cdot 10^5 s + 6.64 \cdot 10^{11}\right)}{(s + 1.374 \cdot 10^6)(s^2 + 1.61 \cdot 10^4 s + 8.38 \cdot 10^8)(s^2 + 1.545 \cdot 10^5 s + 2.55 \cdot 10^{11})(s^2 + 2.2 \cdot 10^5 s + 1.17 \cdot 10^{12})} \tag{64}$$

Equation (64) is too complex for the design of a compensation controller. Thus, it can be simplified by dominant poles and right half plane (RHP) zero as in Equation (65). Though simplified, the accuracy of the open-loop TF is reserved as illustrated in Figure 3.

$$G_{s\_s}(s) = \frac{1.51 \cdot 10^4 \left(s - 5.178 \cdot 10^5\right)}{s^2 + 1.612 \cdot 10^4 s + 8.383 \cdot 10^8} \tag{65}$$
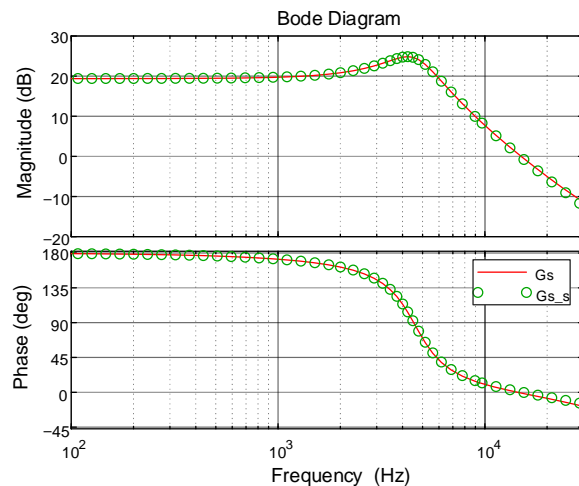

Figure 3. Bode diagram of LLC open-loop TF G_s and simplified TF G_{s_s}.

3. Close-Loop Control of LLC Converter with LED Load

The close-loop control diagram of the LLC LED driving converter is illustrated in Figure 4. As has deduced the output current to normalized switching frequency open-loop TF G_s, the compensation controller G_c can be designed with the desired steady state and dynamic performance obtained. However, in order to promote the reliability and duration of the LLC LED driver, the input large capacitance value electrolytic capacitor has been replaced by a small capacitance value film capacitor, which causes that there is alternate current (AC) voltage ripple in the input DC voltage. As the input DC voltage comes from the front-end rectifier, the frequency of the input AC ripple voltage is two times that of grid voltage f_{ac}. The input AC voltage ripple will cause considerable output current ripple, so the active ripple rejection (ARR) method must be adopted.
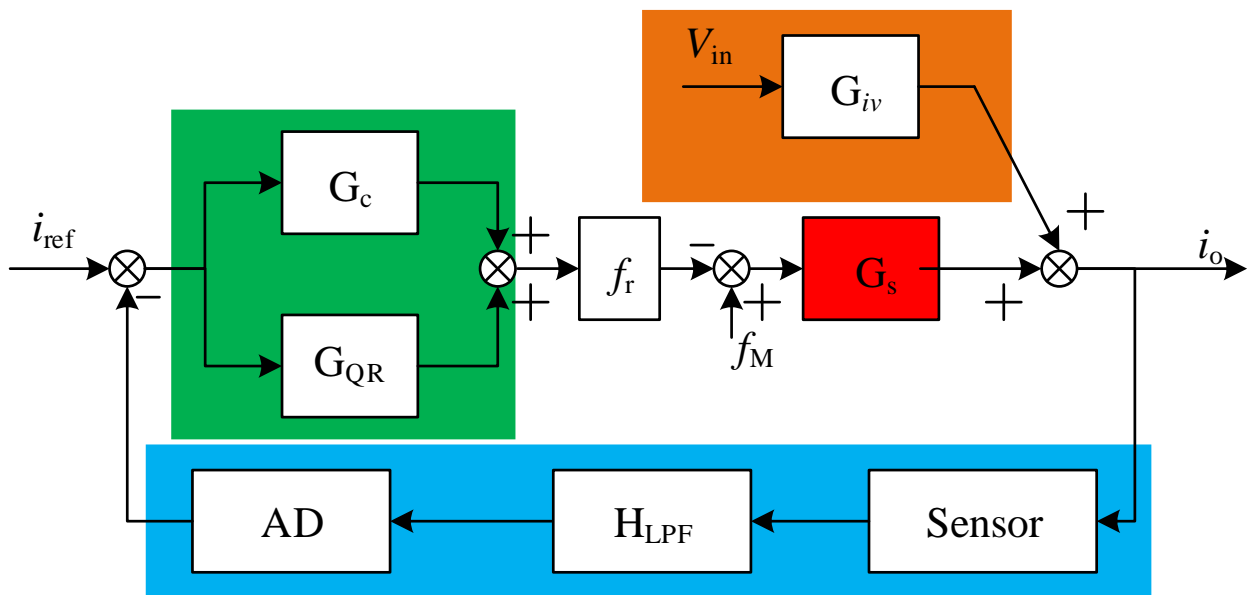
Figure 4. The close control diagram of the LLC LED driver. Box in green represents controller G_c and G_{QR}, Box in blue represent feedback modules, box in red represents deduced output current to normalized frequency transfer function of LLC converter, box in brown represents deduced transfer function G_{iv}.

In order to suppress the input AC voltage-caused output current ripple, a high-gain quasi-resonant controller (QRC) G_{QR} at the frequency of $2f_{ac}$ is adopted. As shown in Figure 4, the QRC is in parallel with the controller Q_c. Controller Q_c takes the role of the average output current regulation and the QRC has a significant effect on the output current ripple rejection.

3.1. Quasi-Resonant Controller-Based ARR

The TF of the QRC is given in Equation (66), in which there are gain k, center angular frequency ω_o and damping ratio ζ as the three control parameters. Setting the center frequency to be $2f_{ac}$ (100 Hz), the Bode diagrams of the QRC under different damping ratios ζ are shown in Figure 5.

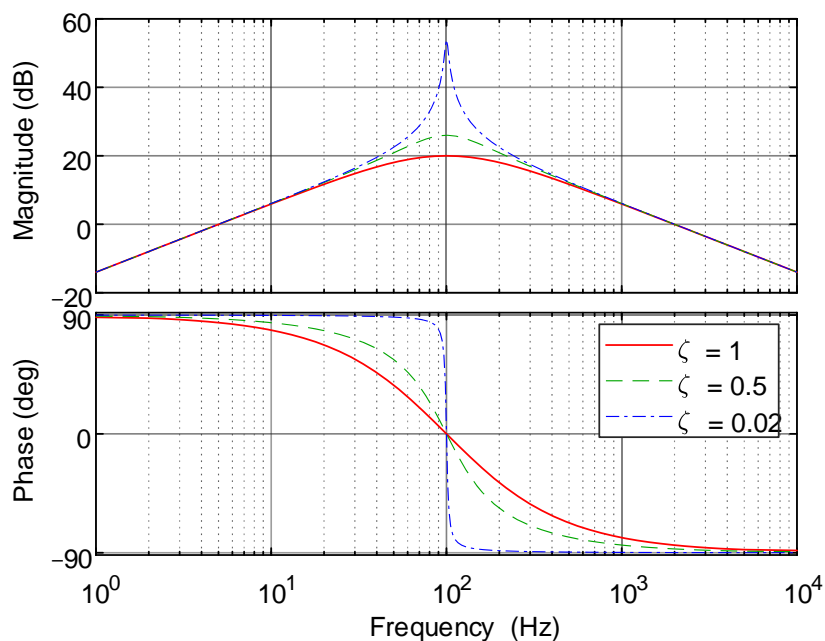$$Q_R(s) = \frac{2k\omega_o s}{s^2 + 2\zeta\omega_o s + \omega_o^2} \tag{66}$$

Figure 5. Bode diagram of QRC under different damping ratios under k = 1.

From Figure 5, the following can be seen:

(1)   The QRC has an adjustable peak amplitude at the center angular frequency ω_o. So, the center angular frequency ω_o of the QRC can be set to be two times the grid voltage frequency to obtain a maximal gain of the input signal.

(2)   The value of the damping ratio has an important influence on the amplitude and passband of the QRC. The smaller the damping ratio is, the larger the peak gain and the narrower the passband. So, the value of the damping ratio should be designed under the balance of peak gain and the passband width.

(3)   Control parameter gain k can promote the gain at the whole frequency range, which is not recommended to be set too large to simplify the design of the compensation controller Q_c.

The control diagram of the QRC is illustrated in Figure 6.
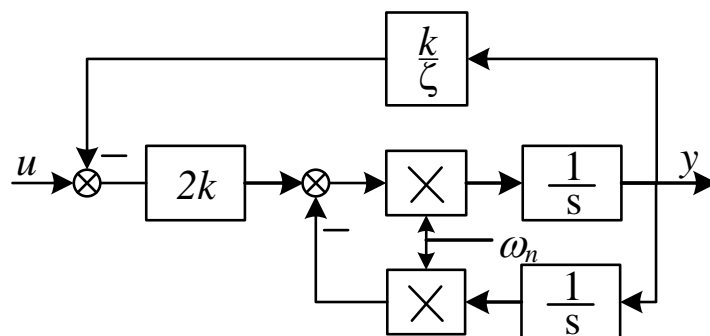
Figure 6. The control diagram of QRC.

If the frequency of the grid voltage is stable, a small damping ratio value can be chosen to have a large enough gain with good output current ripple rejection performance guaranteed. However, in practice, the grid voltage frequency is varying because of the dynamic changing of source and load power. To obtain a good ARR performance, a second-order general integral (SOGI) single-phase SPLL as shown in Figure 7 is adopted to trace the grid frequency.
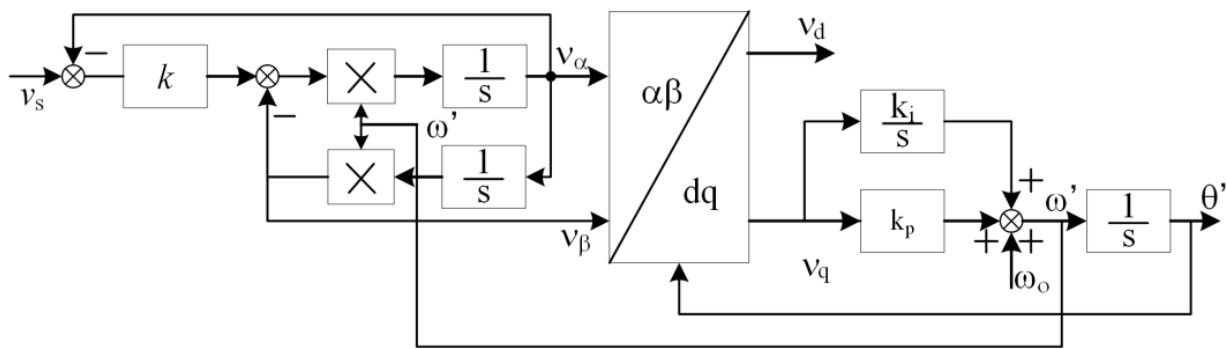
Figure 7. The control diagram of SOGI-based single-phase PLL.

By dynamically changing the center frequency of the QRC according to two times of the SPLL locked grid frequency, the output current ripple can be suppressed to a considerably small level.

3.2. Compensation Controller Design

Now it comes to the design of the compensation controller G_c. The design of controller G_c is based on the deduced simplified open-loop TF given in (2). As can be seen that the system type of (2) should be promoted to be one to eliminate the steady-state error. So, compensator G_c should have an integral element. At the same time, the two dominant poles in (2) will cause too large a declining speed of logarithmic amplitude and phase curves, which is not favorable to stability and dynamic response performance. Thus, two zeros same as that of the dominant poles are added in the compensator G_c. In addition, to suppress the gain at frequency points no less than the switching frequency, a pole at half of the switching frequency is added to G_c. Based on the above compensator design principle, the TF of the controller G_c is given in Equation (67).

$$G_c = \frac{k_c(s^2 + 1.612 \cdot 10^4 s + 8.383 \cdot 10^8)}{8.383 \cdot 10^8 s (2s/\omega_s + 1)} \tag{67}$$

In Equation (67), k_c is the open-loop gain and ω_s is the minimal switching angular frequency. Open loop gain k_c of G_c is designed according to the desired phase margin and amplitude crossover frequency ω_c.

As shown in the close-loop control diagram in Figure 4, to filter out the switching frequency noise, there is a second-order low pass filter (LPF) in the feedback loop and its TF G_{LPF} is given in Equation (68).

$$G_{LPF} = \frac{k_f \omega_f^2}{s^2 + \omega_f/Q + \omega_f^2} \tag{68}$$

In (68), ω_f is the cut-off frequency of the LPF and Q is the quality factor. In the design of the LPF, ω_f is set to be 20 kHz, which is less than half of the analog-to-digital conversion (ADC) sampling frequency to filter out the high-frequency noise and Q is set to be 0.5 to obtain a smooth filtering performance.

By far, the loop gain G_{all} of the LLC LED driving converter can be obtained by multiplying the three TFs shown in Equations (65), (67) and (68). In practical control, the AD sampling frequency is 50 kHz, and the switching frequency equals the resonant frequency of 100 kHz. The Bode diagrams of both TF in Equation (65) and G_{all} are illustrated in Figure 8.
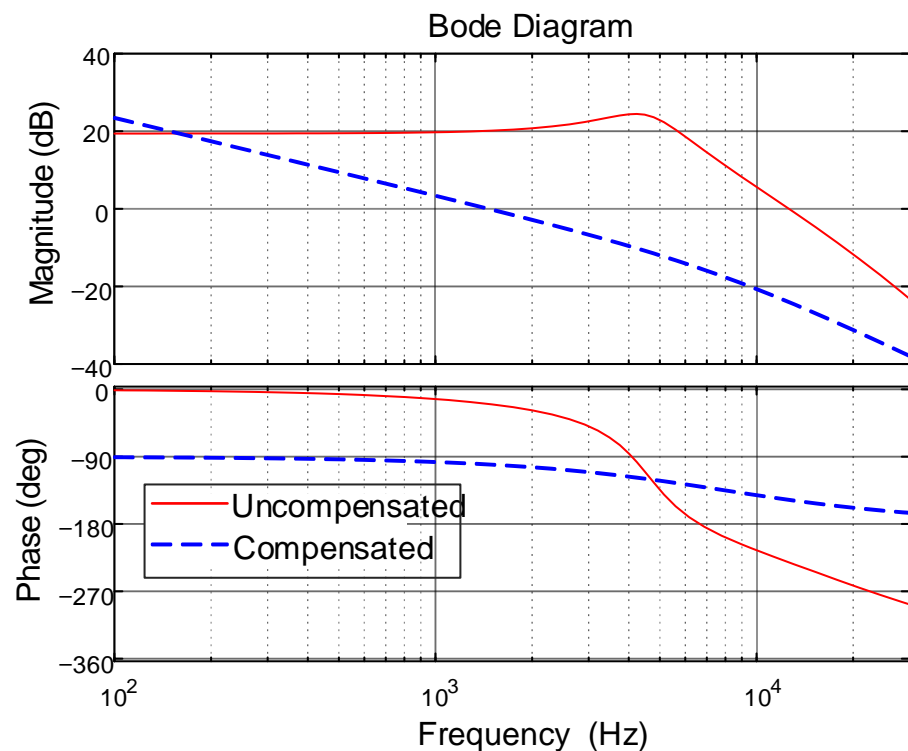
Figure 8. Bode diagrams of both $-G_{s\_s}$ and $-G_{all}$.

From Figure 8, it can be seen that without a compensator, the original control system is unstable. Under the designed compensator, the crossover frequency of the compensated control system is set to be 1.46 kHz with a phase margin of 79.6°. The open-loop gain k_c of the compensator G_c is set to be 1000.

4. Simulation Verification

To verify the correctness and effectiveness of the constructed LLC LED driving converter small signal model, the QRC controller, the SPLL-based output current ripple method and compensation controller design method, the LLC LED driving converter as shown in Figure 1 simulating prototype is constructed in Simulink and the close-loop controller shown in Figure 4 is implemented in the simulation experiment. In the simulation, the input DC voltage Vin is 400 V, and the default input AC voltage is a sine wave with a peak voltage of 40 V and frequency 100 Hz. The control parameters damping ratio and gain of the QRC controller are set to be 0.02 and 1, respectively.

Figure 9 illustrated the output current and voltage waveform under the control of the proposed compensation controller with and without the QRC. Before time 0.12 s, both compensator Q_c and output current ripple rejection controller QRC work, and the output current is controlled to the reference value 1 A with a peak-to-peak current ripple of 80 mA. After 0.12 s, the QRC controller is cut-off and the peak-to-peak output current ripple is increased to 200 mA. Figure 9 has verified the correctness and effectiveness of the compensation controller and output current ripple rejection controller QRC.

In Figure 10, the LLC LED driving converter is controlled with the designed compensator Q_c and ARR controller QRC, and the dynamic output current and voltage are illustrated under dimming conditions. Before 0.08 s, the reference current is 1 A. In the time span from 0.08 to 0.09, the reference current declined linearly from 1 A to 0.75 A. In the time span from 0.09 to 0.12, the reference current keeps being 0.75 A. After that, in the time span from 0.12 to 0.14, the reference current decrease linearly from 0.75 A to 0.35 A once again and stays at 0.35 A.
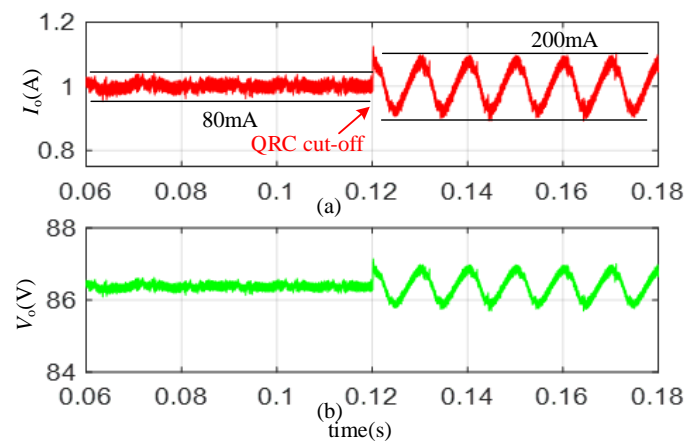
Figure 9. Output (**a**) current and (**b**) voltage under the control of the design compensator Qc with and without QRC. The line in red color represent output current waveform and The line in green color represent output current waveform. The colors make the waveform more clear for reader.
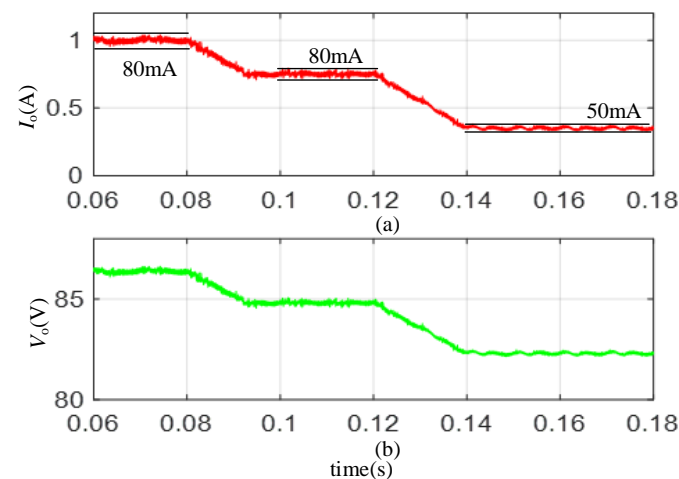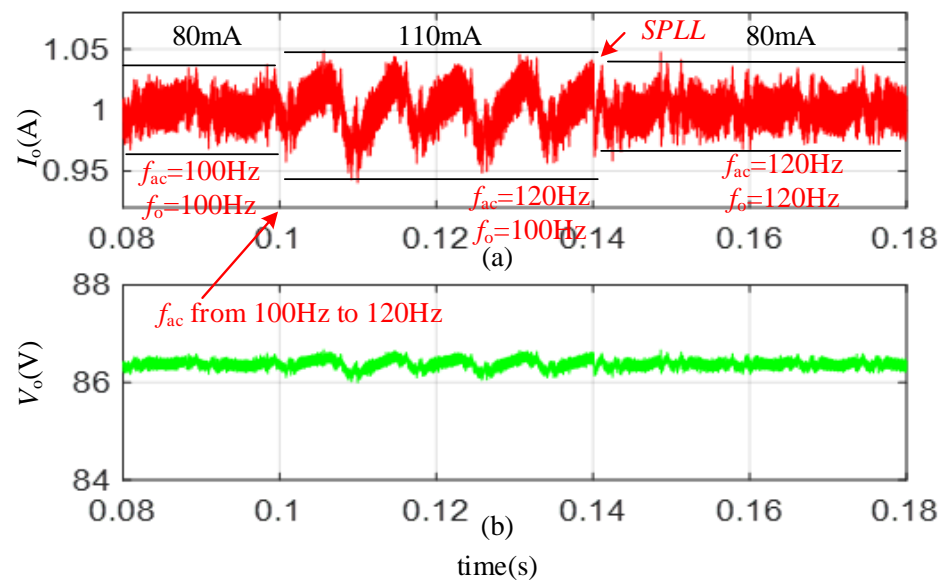

Figure 10. Output (**a**) current and (**b**) voltage under the control of the designed compensator and QRC under diming conditions. The line in red color represent output current waveform and The line in green color represent output current waveform. The colors make the waveform more clear for readers.

From Figure 10, it can be seen that the close-loop controller can closely follow the changing reference current without overshooting. Figure 10 has further verified that the designed compensator and ARR controller can effectively control the output average current and suppress the output current ripple under different current levels and have good dynamic performance.

In Figure 11, before time 0.1 s, the input AC voltage frequency is 100 Hz, while after 0.1 s, the input AC voltage frequency is jumped to 120 Hz. In the time span from 0.1 s to 0.14 s, the center frequency of the QRC controller still keeps 100 Hz, and the output peak-to-peak current ripple is increased from 80 mA to 110 mA because of the gain decreasing of the QRC when the input voltage frequency deviating from the QRC center frequency. Compared with the 200 mA peak-to-peak current ripple shown in Figure 9, it can be seen that the QRC can still suppress the output current ripple at the nearby of its center frequency. After 0.14 s, the center frequency of the QRC is updated to be 120 Hz based on the SPLL locked grid frequency. It can be seen that the output peak-to-peak current ripple is decreased from 110 mA to 80 mA again.

Figure 11. Output (**a**) current and (**b**) voltage under the control of the designed compensator and QRC with and without SPLL. The line in red color represent output current waveform and The line in green color represent output current waveform. The colors make the waveform more clear for readers.

Figure 11 has verified that the SPLL-based QRC can effectively suppress the output current ripple even if the grid voltage frequency deviates from the nominal value, which makes it suitable for the weak power grid with large amounts of new energy penetration.

5. Conclusions

This paper has deduced the small signal model of the traditional power equivalent resistance and the EDF-based LLC LED driving converter and analyzed the effect that LED low internal resistance has on the transfer function. After that, the accurate small signal model with the LED nonlinear model considered is deduced and verified. Based on the deduced accurate small signal LLC model, a compensation controller design method is proposed with desirable steady state and dynamic performance obtained. To suppress the input AC voltage-induced output current ripple, a quasi-resonant is adopted and the control parameter design method is detailed. A single-phase software phase lock loop is adopted to trace the grid voltage frequency deviation to obtain the best active ripple rejection performance. The correctness and effectiveness of the proposed design method have been verified by a large number of simulation experiments.

References

1. Feng, W.; Fred, C.L.; Paolo, M. Optimal trajectory control of LLC resonant converters for LED PWM dimming. *IEEE Trans. Power Electron.* **2013**, *29*, 979–987. [CrossRef]
2. Hayashi, Y.; Toyoda, H.; Ise, T.; Matsumoto, A. Contactless DC connector based on GaN LLC converter for next-generation data centers. *IEEE Trans. Ind. Appl.* **2015**, *51*, 3244–3253. [CrossRef]
3. Demirel, I.; Erkmen, B. A very low-profile dual output LLC resonant converter for LCD/LED TV applications. *IEEE Trans. Power Electron.* **2013**, *29*, 3514–3524. [CrossRef]
4. Wu, J.; Li, S.; Tan, S.-C.; Hui, S.Y.R. Fixed-Frequency Phase-Shift Modulated Capacitor-Clamped LLC Resonant Converter for EV Charging. *IEEE Trans. Power Electron.* **2022**, *37*, 13730–13742. [CrossRef]
5. Watanabe, T.; Kurokawa, F. Efficiency comparison between phase shift and LLC converters as power supply for information and communication equipments. In Proceedings of the 2015 IEEE International Telecommunications Energy Conference (INTELEC), Osaka, Japan, 18–22 October 2015.
6. Simone, S.D.; Adragna, C.; Spini, C.; Gattavari, G. Design-oriented steady-state analysis of LLC resonant converters based on FHA. In Proceedings of the International Symposium on Power Electronics, Electrical Drives, Automation and Motion, 2006. SPEEDAM, Taormina, Italy, 23–26 May 2006.
7. Huang, H. FHA-based voltage gain function with harmonic compensation for LLC resonant converter. In Proceedings of the 2010 Twenty-Fifth Annual IEEE Applied Power Electronics Conference and Exposition (APEC), Palm Springs, CA, USA, 21–25 February 2010.
8. Shaik, M.; Ramesh, K. *Digital Compensator Design for LLC Resonant Converter*; Microchip Technology Inc.: Chandler, AZ, USA, 2012.
9. Yang, B.; Fred, C.L.; Jovanovic, M. Small-signal analysis for LLC resonant converter. *Cpes Seminar* **2003**, *7*, 144–149.
10. Wang, Y.; Gao, S.; Guan, Y.; Huang, J.; Xu, D.; Wang, W. A single-stage LED driver based on double LLC resonant tanks for automobile headlight with digital control. *IEEE Trans. Transp. Electrif.* **2016**, *2*, 357–368. [CrossRef]
11. Menke, M.F.; Seidel, A.R.; Tambara, R.V. LLC LED driver small-signal modeling and digital control design for active ripple compensation. *IEEE Trans. Ind. Electron.* **2018**, *66*, 387–396. [CrossRef]
12. Wang, H.; Blaabjerg, F. Reliability of capacitors for DC-link applications in power electronic converters—An overview. *IEEE Trans. Ind. Appl.* **2014**, *50*, 3569–3578. [CrossRef]
13. Karanayil, B.; Agelidis, V.G.; Pou, J. Performance evaluation of three-phase grid-connected photovoltaic inverters using electrolytic or polypropylene film capacitors. *IEEE Trans. Sustain. Energy* **2014**, *5*, 1297–1306. [CrossRef]
14. Xu, D.; Zhang, J.; Chen, W.; Lin, J.; Lee, F. Evaluation of output filter capacitor current ripples in single phase PFC converters. In Proceedings of the Power Conversion Conference-Osaka 2002 (Cat. No. 02TH8579), Osaka, Japan, 2–5 April 2002; Volume 3.
15. Zhu, J.; Pratt, A. Capacitor ripple current in an interleaved PFC converter. *IEEE Trans. Power Electron.* **2009**, *24*, 1506–1514. [CrossRef]
16. He, L. A novel quasi-resonant bridge modular switched-capacitor converter with enhanced efficiency and reduced output voltage ripple. *IEEE Trans. Power Electron.* **2013**, *29*, 1881–1893.
17. Song, M.-G.; Lee, W.-C. A Study on the Reduction of 120 Hz Ripple Voltage Effect and Current Distortion Rate by the Compensation of Reactive Power on Single-phase Photovoltaic Systems. *J. Electr. Eng. Technol.* **2022**, *17*, 2849–2856. [CrossRef]
18. Akhtar, M.A.; Saha, S. An adaptive frequency-fixed second-order generalized integrator-quadrature signal generator using fractional-order conformal mapping based approach. *IEEE Trans. Power Electron.* **2019**, *35*, 5548–5552. [CrossRef]
19. Kjaer, S.B.; John, K.P.; Frede, B. A review of single-phase grid-connected inverters for photovoltaic modules. *IEEE Trans. Ind. Appl.* **2005**, *41*, 1292–1306. [CrossRef]